Nuclear Inst. and Methods in Physics Research, A 1051 (2023) 168213

Contents lists available at ScienceDirect

Nuclear Inst. and Methods in Physics Research, A

journal homepage: www.elsevier.com/locate/nima


NUCLEAR INSTRUMENTS & METHODS IN PHYSICS RESEARCH

Full Length Article

Simulations and analysis tools for charge-exchange (d, ^{2}He) reactions in inverse kinematics with the AT-TPC

S. Giraud [a,*], J.C. Zamora [a,*], R.G.T. Zegers [a,b], Y. Ayyad [c], D. Bazin [a,b], W. Mittig [a,b], A. Carls [a,b], M. DeNudt [a,b], Z. Rahman [a,b]

[a] Facility for Rare Isotope Beams, Michigan State University, East Lansing, MI 48824, USA
[b] Department of Physics and Astronomy, Michigan State University, East Lansing, MI 48824-1321, USA
[c] IGFAE, Universidade de Santiago de Compostela, E-15782 Santiago de Compostela, Spain

ARTICLE INFO

Keywords:
AT-TPC
Charge-exchange reactions
Simulation
(d,^{2}He)

ABSTRACT

Charge-exchange (d,^{2}He) reactions in inverse kinematics at intermediate energies are a very promising method to investigate the Gamow–Teller transition strength in unstable nuclei. A simulation and analysis software based on the ATTPCROOT package was developed to study this type of reactions with the active-target time projection chamber (AT-TPC). The simulation routines provide a realistic detector response that can be used to understand and benchmark experimental data. Analysis tools and correction routines can be developed and tested from simulations in ATTPCROOT, because they are processed in the same way as the real data. In particular, we study the feasibility of using coincidences with beam-like particles to unambiguously identify the (d,^{2}He) reaction channel, and to develop a kinematic fitting routine for future applications. More technically, the impact of space-charge effects in the track reconstruction, and a possible correction method are investigated in detail. This analysis and simulation package constitutes an essential part of the software development for the fast-beams program with the AT-TPC.

1. Introduction

During the last few decades, Time Projection Chambers (TPC) have been successfully used as large-volume tracking detectors in many particle physics experiments, e.g., TOPAZ [1], STAR [2] or ALICE [3]. However, in the recent years, the operation of TPCs in Active Target (AT) mode have gained a great interest in the nuclear physics community. This type of devices allow the use of a target medium as a tracking-detection system with a large solid angle coverage and low-energy detection thresholds, which make them ideal for experiments with rare-isotope beams in inverse kinematics.

Currently, many facilities around the world are investing a great effort in the development of active target TPCs as a fundamental part for future research programs [4–9]. One of these projects is the already operating Active-Target Time Projection Chamber (AT-TPC) [8] at the Facility for Rare Isotope Beams (FRIB). The AT-TPC has a cylindrical geometry with dimensions of ~125 cm × ~ø 75 cm. The gas volume is enclosed by a cathode plate and a Micromegas electron amplifier plate, as shown in Fig. 1, which represents an active volume of 100 cm × ø 58 cm. The system is designed to take the beam particles impinging along the symmetry axis of the active volume and to detect the nuclear reactions induced in their path. The beam particles and the reaction products ionize gas atoms while traversing the active volume and generate ionization electrons. Upon applying a uniform electric field, ionization electrons produced by charged particles along their tracks drift towards the Micromegas plane at a constant velocity. The high segmentation of the Micromegas ($\sim 10^4$ triangular pads) makes it possible to obtain the energy loss and a two-dimensional image of the track, while the third dimension (along the beam axis) is taken from the drift time of the electrons. A hole (ø 3 cm) in the central part of the Micromegas plane creates an insensitive region around the beam axis that allows relatively high beam intensities (see Fig. 1). This is important for performing experiments in combination with a magnetic spectrometer that enables measurements of heavy residues in coincidence with the tracks in the AT-TPC. The active region of the AT-TPC is separated from the vacuum of the beam line and the spectrometer by 12 μm polyamide windows.

Charge-exchange ($d,{}^2$He) reactions at intermediate energies are well known to be a strong Gamow–Teller (GT) transition filter ($\Delta T, \Delta S = 1$) from experiments in forward kinematics [10–14]. The ($d,{}^2$He) probe in inverse kinematics is a very promising method for measuring the GT transition strength in unstable nuclei, which can be used, e.g., to constrain stellar electron-capture rates and determine the nuclear structure far from stability [15]. The output channel, ^{2}He, is an unbound system that decays into two protons. In order to achieve this type of

---

* Corresponding author.
E-mail addresses: giraud@frib.msu.edu (S. Giraud), zamora@frib.msu.edu (J.C. Zamora).

https://doi.org/10.1016/j.nima.2023.168213
Received 2 November 2022; Received in revised form 13 February 2023; Accepted 13 March 2023

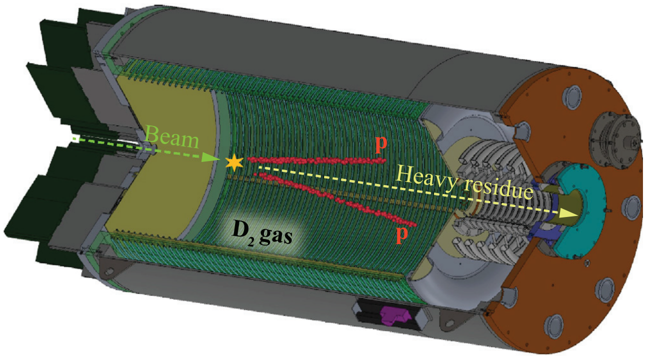

Fig. 1. Schematic view of the AT-TPC with a $(d,{}^{2}\text{He})$ reaction. The active volume, filled with a pure deuterium (D_2) gas, constitutes a cylindrical chamber of 100 cm long with a diameter of 58 cm. The beam impinges along the central axis. The Micromegas plane (upstream) and the cathode plane (downstream) have a hole in the central region that allows the beam to enter and the heavy residue to exit the AT-TPC. The electric field is applied along the beam axis direction.

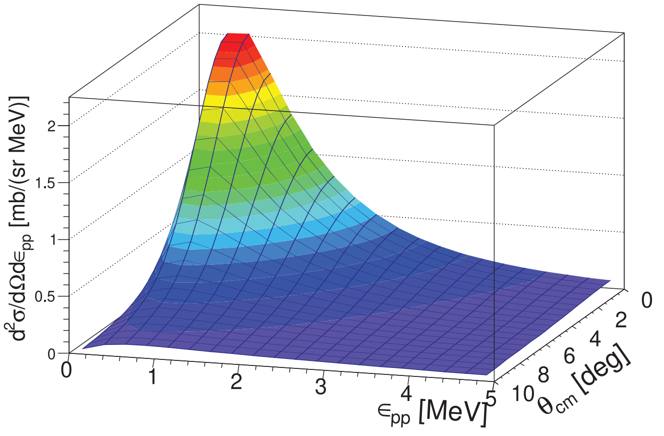

Fig. 2. Double-differential cross section of the reaction ${}^{14}\text{O}(d,{}^{2}\text{He}){}^{14}\text{N}$ at 100 MeV/u (populating the ${}^{14}\text{N}$ 1_1^+ state at 3.9 MeV) as a function of the scattering angle ($\theta_{\text{c.m.}}$) and the relative energy (ε_{pp}). This cross section was calculated using the code ACCBA [21].

experiments with unstable beams, it is necessary to operate the AT-TPC with a pure deuterium gas, which is used as a target and a tracking medium for the two protons originating in the output channel of the $(d,{}^{2}\text{He})$ reactions. The detection of two protons with the same vertex in the AT-TPC gives the possibility to reconstruct the missing mass energy and the scattering angle of the ${}^{2}\text{He}$ particle.

In this work, we have developed a simulation and analysis software based on the ATTPCROOT package [16,17] to study $(d,{}^{2}\text{He})$ experiments with the AT-TPC. The simulations offer an ideal method to benchmark and to understand the experimental data taken with this system. The realistic detector response provided by the simulations enables a testing method for the analysis tools that are applied to the experimental data. This paper is organized as follows: in Section 2, we give an overview of the simulation routines implemented in this work, Section 3 shows a few remarkable advantages of using coincidences with beam-like particles, space-charge effects and a correction method are discussed in Sections 4, and 5 presents the conclusions.

2. Simulation of $(d,{}^{2}\text{He})$ reactions

Simulation routines of $(d,{}^{2}\text{He})$ reactions were developed using the ATTPCROOT package [16,17] written in the C++ programming language. ATTPCROOT uses the FAIRROOT framework [18] which was developed for the analysis of experiments at FAIR and later redesigned for other experimental setup. The ATTPCROOT package provides consistent analysis tools for both simulated and experimental data. The simulation part of this package comprises three main stages: event generator, digitization and reconstruction. The latter stage is also common for the data analysis part of the package.

2.1. Event generator

The simulation events are generated with the Virtual Monte-Carlo (VMC) package [19] that serves as an interface to the GEANT4 toolkit [20]. The sensitive volume of the AT-TPC is defined as a cylindrical geometry filled with a deuterium gas (D_2) that serves simultaneously as target and tracking medium for the charged particles involved in the reaction. Thus, the event generator class creates the particles that are transported by GEANT4 and stores the hit information in a class that handles the simulated data points.

The $(d,{}^{2}\text{He})$ events are generated along the active volume using a realistic beam emittance based on the ion-optical properties of the beam line at the S800 spectrometer at FRIB [22]. Three particles are produced in the final channel of each reaction: two protons (from the ${}^{2}\text{He}$ decay) and an ejectile. A routine to simulate the in-flight decay of the residues after the reaction is also included in the code. In order to have a consistent treatment of the $(d,{}^{2}\text{He})$ reaction, a relativistic three-body kinematics is used to generate the particles in the output channel. An important part of the $(d,{}^{2}\text{He})$ kinematics is the description of the relative energy between the two protons (ε_{pp}) in the ${}^{2}\text{He}$ frame. ε_{pp} is calculated with the code ACCBA (Adiabatic Coupled-Channels Born Approximation) [21], which has been successfully used to reproduce $(d,{}^{2}\text{He})$ data from experiments in forward kinematics [13,23,24]. Fig. 2 shows the double-differential cross section for the ${}^{14}\text{O}(d,{}^{2}\text{He}){}^{14}\text{N}$ reaction (populating the ${}^{14}\text{N}$ 1_1^+ state at 3.9 MeV) as a function of ε_{pp} and $\theta_{\text{c.m.}}$ (center-of-mass angle) calculated with the code ACCBA. As expected for a GT transition, the differential cross section peaks at forward scattering angles. The relative energy between the two protons ε_{pp} is distributed from 0 up to 5 MeV. These angular and energy distributions are included as an input to the event generator to accordingly determine the detection efficiency as a function of $\theta_{\text{c.m.}}$ and ε_{pp}.

2.2. Digitization

The digitization stage uses the generated tracks and simulates the detector response. This part is divided in two subroutines: electron diffusion and electronics response. In the electron diffusion subroutine, the number of ionization electrons is calculated for every hit based on the energy deposition and the average ionization energy for the gas target. Subsequently, the drift time of the electrons to reach the pad plane is calculated using a drift velocity obtained from MAGBOLTZ [25], which simulates the electron transport in a certain gas under the influence of an electromagnetic field. It is important to mention that the uncertainty on the reconstructed excitation energy of the ejectile depends on the electron diffusion in the gas volume, and on the straggling (angle and energy) of the protons. For example, a large diffusion parameter produces thicker proton tracks which degrades the fitting precision. The corresponding parameters were set to realistic values achieved with the AT-TPC operated with a pure D_2 gas. Effects on the electron drift due to field distortions can be simulated in detail by using electron transport routines in this method, as explained in Section 4. Fig. 3 shows an example of a simulated $(d,{}^{2}\text{He})$ event and its respective projection on the pad plane, and Fig. 4(a) shows the 3D reconstruction of an event. Each proton hit produces an electron cloud that drifts in the gas volume towards the detector pixels in the pad plane. In particular, measurements of proton tracks in the AT-TPC require a high gain in the electronics, which can enhance also the detection of δ-rays. The output of this subroutine is coupled to

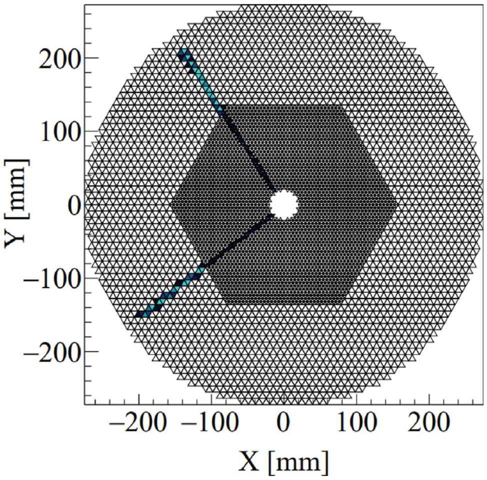

Fig. 3. A projected signal on the micromegas plane of a simulated $(d,{}^2\mathrm{He})$ event with the AT-TPC. Note that the pad plane has a 3 cm aperture in the central region that allows the beam-like particles pass through the active volume.

the electronics response module that simulates a signal for each pad. In this part, an electron avalanche generates a pulse shape by using a realistic response of the Micromegas, with the gain obtained from a Polya distribution, and the GET (general electronics for TPCs) [26] system.

2.3. Reconstruction

The event reconstruction and further tasks are the same for both simulated and experimental data. After the digitization, a point cloud (collection of hits in the 3D space) for each reaction in the gas volume is extracted. The analysis of these point clouds is performed with a pattern recognition and fitting routine that searches $(d,{}^2\mathrm{He})$ events and extracts the kinematical information such as scattering angle, momentum, and excitation energy. Tracking algorithms allow to identify the points that belong to the particle tracks (inliers) within a entire point cloud and reject the noise points (outliers). A tracking algorithm based on RANSAC (RANdom SAmple Consensus) has been successfully employed to analyze data from the AT-TPC [27]. However, RANSAC is rather sensitive to the inlier–outlier threshold and it requires a prior parameter fine tuning each time for a specific application. Also, a common problem of the algorithm is that it fails when describing data that contain multiple structures, such as point clouds with several tracks that have a significant amount of pseudo-outliers. A few improved versions of RANSAC-like algorithms were developed for the reconstruction of $(d,{}^2\mathrm{He})$ events [28]. In these routines, the process of model verification is optimized by using a probabilistic approach. For instance, the candidate trajectories (model hypotheses) are evaluated on basis of an error probability distribution. This reduces the outlier sensitivity of RANSAC and provides a more robust method to identify particle tracks in point clouds with a large fraction of outliers. Also, a modification in the sampling process based on the relative distance and deposited charge was included to preferentially generate more useful RANSAC hypotheses. The random sampling is constructed in a way that neighboring points are selected with higher probability by assuming a Gaussian distribution for the relative distance between points. Similarly, a probability density distribution using the total charge of the point cloud allows to select more efficiently the points that have a larger energy deposited in gas [28]. Finally, the tracking algorithm is coupled to a least squares routine that improves the RANSAC output and provides a better estimate of the reaction vertex and scattering angles.

For $(d,{}^2\mathrm{He})$ experiments, the AT-TPC operates without a magnetic field. Thus, the particle tracks are 3D line trajectories. The tracking algorithm fits all particle tracks in each event and identifies $(d,{}^2\mathrm{He})$ reactions as two protons emitted with the same vertex (see Fig. 1). The momenta of the recoiling protons ($\boldsymbol{P}_{px}$ with $x = 1,2$) are extracted by combining the track fitting result and the respective track length. The proton energy in the gas can be directly extracted from stopping power tables calculated with the code SRIM [29]. This information is sufficient for the reconstruction of a ^{2}He particle. The first step is to obtain the momentum of ^{2}He from the proton tracks

$$\boldsymbol{P}_{{}^2\mathrm{He}} = \boldsymbol{P}_{p1} + \boldsymbol{P}_{p2}. \tag{1}$$

Then, the relative energy between the two protons is extracted from the invariant-mass calculation in the ^{2}He frame

$$\varepsilon_{pp} = \sqrt{E^2_{{}^2\mathrm{He}} - \boldsymbol{P}^2_{{}^2\mathrm{He}}} - 2m_p, \tag{2}$$

where $E_{{}^2\mathrm{He}}$ is the total energy of the ^{2}He particle and m_p the proton mass.

To ensure that two protons are in the spin–singlet (${}^1\mathrm{S}_0$) state [30], and the $(d,{}^2\mathrm{He})$ reaction proceeds exclusively with the transfer of spin $\Delta S = 1$, it is preferred to constrain the analysis to small values of ε_{pp}. In forward kinematics experiments, the two protons from ^{2}He are analyzed with a magnetic spectrometer, therefore small values of ε_{pp} are selected by the limited acceptance of the spectrometer or through software cuts in the measured ε_{pp} distribution [10,14,31]. However, in inverse kinematics, the integrated ε_{pp} range depends on the detection efficiency and acceptance of the detector system. At small $\theta_{\mathrm{c.m.}}$ the momentum transfer of the reaction is also small, resulting in a low kinetic energy of the virtual ^{2}He particle. Consequently, the two protons from the decay of ^{2}He will also have small kinetic energies. The reconstruction of the ^{2}He particles is limited by the size of the insensitive region of the AT-TPC (see Fig. 3). In this case, the two proton tracks are detected when the relative energy ε_{pp} is sufficiently high. This is shown in Fig. 4(b): relative energies between 1 and 2.5 MeV are probed for $\theta_{\mathrm{c.m.}} \approx 0°$. At larger $\theta_{\mathrm{c.m.}}$, the momentum transfer increases, which is reflected in larger kinetic energies for the ^{2}He particle (also for the two protons). If the energy of the two protons becomes too high, they escape from the active volume of the AT-TPC and the reconstruction of the event is not possible. Therefore, at high $\theta_{\mathrm{c.m.}}$, only events with $\varepsilon_{pp} \lesssim 1$ MeV can be reconstructed, as shown in Fig. 4(b). As the differential cross section for a particular transition depends on both $\theta_{\mathrm{c.m.}}$ and ε_{pp} (see Fig. 2), a ε_{pp} acceptance correction as a function of $\theta_{\mathrm{c.m.}}$ must be taken into account for extracting the differential cross section and the GT transition strength. The simulations presented here are essential for this correction.

Once the ^{2}He particle is reconstructed, a missing-mass calculation is performed to extract the excited states populated in the reaction. In this calculation, the angle and the energy of the incident nucleus are fixed to average values. With beam tracking detectors, the angle and the energy of the incident nucleus can be measured on an event-by-event basis, improving the precision of the missing-mass calculation. Fig. 4(c) shows the reconstructed kinematic plot for the ${}^{14}\mathrm{O}(d,{}^2\mathrm{He}){}^{14}\mathrm{N}$ reaction ($Q_{\mathrm{g.s.}} = 3.7$ MeV) and its respective projection in the missing mass (Fig. 4(d)). Simulations of $(d,{}^2\mathrm{He})$ reactions populating the ground state (g.s.) and excitation energies of 10 and 20 MeV are assumed in order to test the reconstruction routines.

The broadening of the kinematic lines is not only due to the energy and angle resolutions of the reconstruction, the distribution of the internal ^{2}He energy also contributes to it (e.g., about ∼30% in the g.s. Fig. 4(c)). The reconstructed scattering angle and kinetic energy of the ^{2}He particle at $E_x = 10$ MeV (see Fig. 4(c)) seems to deviate from two-body kinematics calculation at $\theta_{cm} \gtrsim 6°$, this is explained by the limited acceptance at large scattering angles (Fig. 4(b)) and the resolution of the reconstruction. The resolution of the excitation-energy peaks (Fig. 4(d)) depends on the kinematics of the reaction. For instance, the resolution of the ground-state transition in the present example is dominated by the uncertainty in the reconstructed scattering angle of the ^{2}He particle, whereas at higher excitation energies the resolution

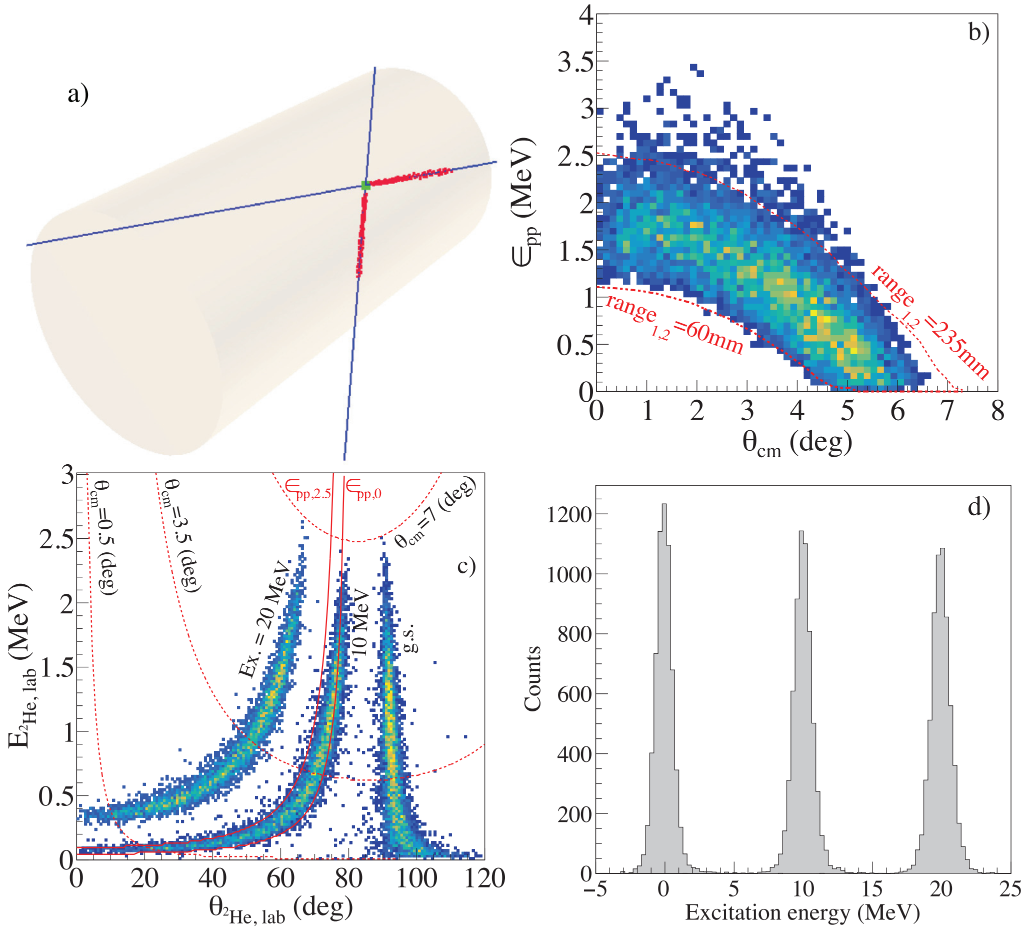

Fig. 4. (a) Simulated ^{14}O(d, ^{2}He)^{14}N event, at a beam energy of 100 MeV/u and D_2 gas at 530 Torr, with the respective track fitting and vertex reconstruction. (b) Internal energy of ^{2}He as function of the center-of-mass scattering angle. The red dashed lines indicate the particle ranges of 60 mm and 235 mm, respectively. The points above the 235 mm range correspond to tracks with scattering angles different than 90°. (c) Kinematics for the ^{14}O(d, ^{2}He)^{14}N reaction, reconstructed ^{2}He scattering angle as function of ^{2}He kinetic energy. Three excited states in ^{14}N were assumed in this example: E_x = 0, 10 and 20 MeV. The red lines are theoretical kinematics lines at 10 MeV excitation energy for ϵ_{pp} values of 0 and 2.5 MeV. The red dashed lines indicate center-of-mass scattering angles (0.5°, 3.5° and 7°). (d) Reconstructed missing mass (excitation energy) of ^{14}N, for ground state, 10 and 20 MeV inputs. The distributions were normalized. The peak at 10 MeV has a full width at half maximum (FWHM) of about 1.6 MeV.

depends on both the kinetic energy and the scattering angle. The large acceptance of the AT-TPC provides a good kinematical reconstruction on almost the entire angular range. Due to the relative good angular resolution (better than 1.5° in θ_{lab}) achieved by the tracking algorithm, the excited states are easily separable up to about 8° in the center-of-mass system with an energy resolution of about 1.6 MeV (FWHM).

3. Coincidences with beam-like particles

Complete kinematics measurements including the detection of beam-like particles provide a strong selectivity of the reaction mechanism and also reduce significantly the background in the experimental data. Therefore, a routine that includes a phase-space generator was implemented to properly simulate the in-flight decay and momentum of the residues. Given that the beam-like particles punch through the AT-TPC volume across the central hole of the pad plane, the active target can be mounted at the entrance of the S800 spectrometer at FRIB [22]. Then, $(d,{}^2\text{He})$ events in the AT-TPC can be correlated with the respective particle identification in the spectrometer focal plane detectors. For instance, Fig. 5(a) shows the simulated dispersive and non-dispersive angles of the beam-like particles accepted in the S800 spectrometer assuming an incident ^{14}O beam at 100 MeV/u. Also, it is possible to obtain the magnetic rigidity ($B\rho$) of the accepted residues from the momentum. Fig. 5(b) shows the simulated $B\rho$ distributions for the $^{14}\text{O}(d,{}^2\text{He})^{14}\text{N}$ reaction including several decay channels such as p, n, np and α.

The identification of a beam-like particle in coincidence with two protons emerging from the same vertex is a stringent condition that suppresses the background. As discussed before, δ-rays are expected to be a significant contribution in the point clouds. These points are an important source of background that can lead to a wrong identification of $(d,{}^2\text{He})$ events. In this case, the integrated charge and number of points of each track are substantially smaller than the ones expected for a real proton track. Fig. 6 (insert) shows that these spurious tracks are easily suppressed by the integrated charge condition. Random coincidences due to multiple-scattering events or scattering close to a $(d,{}^2\text{He})$ reaction vertex can also be a source of background. However, the probability of occurrence for such events is very small, even for beam rates at the level of $R = 10^6$ pps. For example, the probability to have an elastic scattering [$^{14}\text{O}(d,d)$] event during a time window of $W = 100 \times 10^{-6}$ s (typical drift time of the electrons for a $L = 100$ cm long drift volume) can be modeled by assuming a Poisson probability distribution with $\lambda = L\rho\sigma W R \approx 8.7 \times 10^{-3}$. In this case, $\rho \approx 1.74 \times 10^{19}$ cm^{-3} is an estimate value of the density of atoms in the gas target, and the scattering cross section $\sigma \sim 50 \times 10^{-27}$ cm^2 ($\theta_{\text{c.m.}} \lesssim$ 8 deg). Using the Poisson distribution with this information, one finds

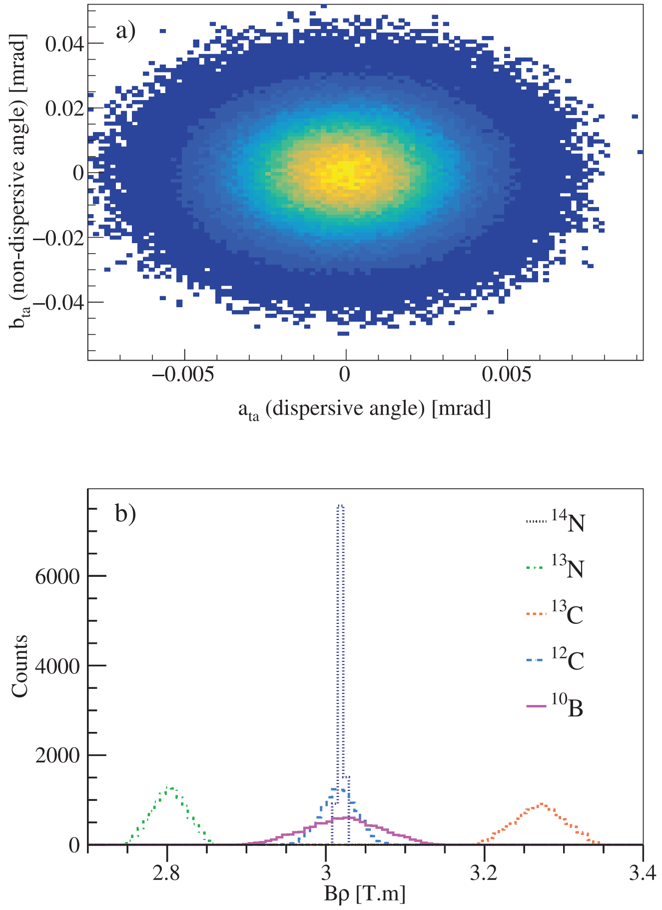

Fig. 5. (a) Simulated dispersive and non-dispersive angles of the ejectiles in the ^{14}O(d, ^{2}He)^{14}N reaction at the target location. (b) Magnetic rigidity of the ejectiles ^{14}N and several decay products.

that the probability to have at least one deuteron elastically scattered within the same time window of a $(d,{}^{2}\mathrm{He})$ reaction is in the order of 1%. Therefore, the background contribution due to an accidental detection of two deuterons elastically scattered, with vertices within ~1 cm [similar condition as the two protons of a $(d,{}^{2}\mathrm{He})$ reaction], is reduced by a factor 100, which makes this source of background negligible.

3.1. Kinematic fitting

In complete kinematic measurements, the resolution of the reconstructed quantities can be improved by using a mathematical procedure called kinematic fitting (KF). KF is a widely used technique in high-energy physics [32,33]. Recently, this method has been proposed for the analysis of nuclear reactions at low energy [34]. The goal of the kinematic fitting is to reduce the uncertainties from the measured quantities by a χ^2 minimization of the reaction kinematics using a few constraints such as the momentum and energy conservation. The solution method implemented in this work is based on the kinematic fitting programs FIT70 [35] and KWFIT [32,33].

In the particular case of a $(d,{}^{2}\mathrm{He})$ reaction, the input channel corresponds to a projectile and a deuterium target, while the output channel is composed by two protons and an ejectile. Each particle have a four-momentum $\alpha_i = (p_{xi}, p_{yi}, p_{zi}, E_i)$ vector that is extracted from the observables of an experiment. The deuteron target is at rest in the laboratory frame, and therefore, this information is only included as a reaction constraint. Let α represent the column vector that contains the four-momentum vectors of the projectile and the three particles in the output channel

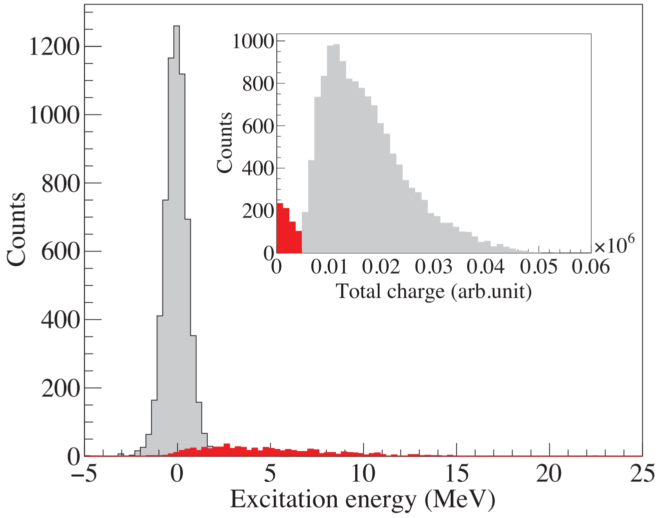

Fig. 6. Reconstructed ^{14}N ground-state energy distribution in the $(d,{}^{2}\mathrm{He})$ reaction (gray peak). The contribution due to stochastic noise fitting is shown in red. The inserted plot represents a distribution of the integrated charge per track and the small bump below 0.005×10^{6} (arb. unit) is associated to the red background in the excitation energy distribution.

$$\alpha = \begin{pmatrix} \alpha_1 \\ \alpha_2 \\ \alpha_3 \\ \alpha_4 \end{pmatrix} \tag{3}$$

The four constraint equations assumed in the KF are the momentum (3D) and the total energy conservation, they can be written as

$$\mathbf{H}(\alpha) \equiv 0, \quad \text{where} \quad \mathbf{H} = (H_1, H_2, H_3, H_4). \tag{4}$$

The equation of above can be expanded around a convenient point α_A that produces a set of linear equations [32,33]

$$0 = \frac{\partial \mathbf{H}(\alpha_A)}{\partial \alpha}(\alpha - \alpha_A) + \mathbf{H}(\alpha_A) = \mathbf{D}\delta\alpha + \mathbf{d}, \tag{5}$$

where $\mathbf{D}$ is a matrix of dimension 4 × 4 that contains the partial derivatives of the constraint parameters $D_{ij} = \frac{\partial Hi}{\partial \alpha_j}$, and $\mathbf{d}$ is a vector of constraints evaluated at the point α_A. The fitting technique is based on the Lagrange multipliers method, in which the χ^2, given by

$$\chi^2 = (\alpha - \alpha_0)^T V_{\alpha 0}^{-1}(\alpha - \alpha_0) + 2\lambda^T(\mathbf{D}\delta\alpha + \mathbf{d}), \tag{6}$$

is minimized. Here, $V_{\alpha 0}$ is the covariance matrix and λ is a vector of Lagrange multipliers. A routine for minimizing Eq. (6) was implemented in the code. The resulting parameters α are improved (compared to the input values α_0) by the momentum and energy constraints of the reaction. In order to avoid problems with the reconstruction of relative energy ε_{pp}, an anticorrelation between the two protons in the output channel was defined in the covariance matrix. This means, the covariance elements of the proton energies were set to −1 to keep the relative energy the same. The KF was tested with the reconstruction of two peaks at 5 and 10 MeV, as shown in Fig. 7. Nuclear excited states can be reconstructed by constraining the ejectile mass in energy intervals. As the beam particles interact with the gas in the insensitive region, no information of the beam momentum is possible to be extracted from the point clouds. For the KF, it was assumed the beam particle impinging the AT-TPC in the normal direction with a momentum resolution (defined in the covariance matrix) of 0.1%. The momentum of the ejectile particle was extracted directly from the event generator with the respective acceptance provided by the

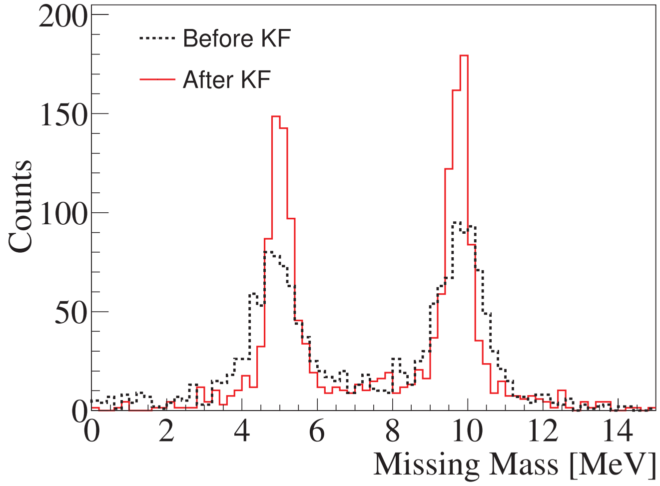

Fig. 7. Missing-mass reconstruction before (dashed line) and after (solid line) the kinematic fitting. Arbitrary states at 5 and 10 MeV excitation energy were assumed to demonstrate the performance of the technique.

S800 spectrometer, as shown in Fig. 5. As explained in Section 2.3, the energy resolution achieved from the tracking is about 1.6 MeV, but with the kinematic fitting the resolution is improved to a value of 0.8 MeV. Thus, the minimization routine corrects for the uncertainty in the energy and angles of the proton tracks by using energy and momentum conservation. Therefore, a significant improvement in the reconstruction of the invariant mass is expected for complete kinematic measurements. The KF routine presented here can also be implemented in the analysis of future experiments. In this case, it might be required the use of tracking detectors before the AT-TPC in order to extract with a better precision the projectile momentum and reaction vertex. Also, it would be necessary to investigate in more detail the reconstruction of virtual particles emerging from the decay of the residues of $(d,{}^2\mathrm{He})$ reactions.

4. Space-charge effects

4.1. Charge build-up

Space-charge effects due to ion accumulation inside the AT-TPC are expected to be present at high beam intensities. A large number of electron-ion pairs $[N(r,z)]$ are produced in the gas volume along the beam path. While electrons drift relatively fast (tens of ∼ μs) to the pad plane, the drift time of ions is a few orders of magnitude slower. It means that the beam is continuously ionizing the gas target producing a charge build-up in the central region of the AT-TPC. This accumulated charge can produce a distortion of the electric field and also affect the electron drift. Experimental evidences of such space-charge effects in the AT-TPC have recently reported [36]. Assuming a constant beam rate R, the production rate of electron-ion pairs per unit volume can be roughly approximated by

$$\dot{N} = \left(\frac{dE}{dx}\right)\frac{R}{wA}, \tag{7}$$

where $\left(\frac{dE}{dx}\right)$ is the beam stopping power in the gas, A is the beam spot area and $w = 37$ eV is the mean ionization energy for D_2 [37]. The charge density in the AT-TPC volume at a time t is given by [38]

$$\rho(x,y,z,t) = \int_0^t e\dot{N}(x,y,z,t')dt', \tag{8}$$

with e the electric charge unit. As an example, a ^{56}Ni beam at 100 MeV/u and rate of 10^5 pps interacting with the AT-TPC filled with a deuterium gas at 500 Torr are assumed. A realistic beam profile of a Gaussian distribution of $\sigma = 0.5$ cm is assumed. The accumulated charge density after an integration time of $t_{\mathrm{max}} = L/u^+$ (L is the AT-TPC length and u^+ is the ion drift velocity) can yield up to 3 pC/cm^3 around the beam axis, as is shown in Fig. 8(a). In order to have a rough estimation of the electric field produced by this charge density, a radial field component is calculated using Gauss' law in the approximation of an infinite cylinder

$$E(r) = \frac{e}{\varepsilon_0}\left(\frac{dE}{dx}\right)\frac{Rt_{\mathrm{max}}}{w}\left(\frac{1-\exp\left(-\frac{r^2}{2\sigma^2}\right)}{r}\right), \tag{9}$$

where ε_0 is the vacuum permittivity. A more rigorous solution can be obtained by integrating the corresponding Green's function, as explained in Ref. [39]. The resulting effect of this field component is a distortion of the electron drift distance. In order to evaluate such effects, it is necessary to simulate the electron transport by solving the Langevin equation numerically [38,39]. An electron transport routine was implemented in the code in the pre-digitization module. An example of a $(d,{}^2\mathrm{He})$ reaction in a distorted electric field is shown in Fig. 8(b). As can be noticed, the tracks are mostly affected in the central region of the AT-TPC. These space-charge effects may cause problems in the event reconstruction, in particular, for the extraction of scattering angles and reaction vertex. The radial distortion is defined as the relative distance between the projected initial point of the electron (x_0,y_0) and the final point on the pad plane (x_f,y_f). Depending on the drift distance, the radial distortion can increase because of the electron transport. For instance, one can see the distortion at different initial distances relative to the Micromegas (drift distance) in Fig. 8(c). In addition, the space-charge effects are stronger near the beam axis, and they become negligible for electrons produced close to the radial edge of the TPC, at r ≈25 cm. For an initial distance of $r = 5$ cm, the distortion can be as big as 3 cm, after a drift distance of 100 cm, which is approximately the equivalent distance of 6 pads. The space-charge effects have also a significant dependence on the beam particle due to the amount of electrons produced in the beam energy loss. The higher the beam charge, the stronger the radial distortion is. Fig. 8(d) shows an example of the radial distortion at $r = 10$ cm for different beams. As expected, the space-charge effects are higher for ^{56}Ni which are about a factor 4 stronger than for ^{24}Mg.

4.2. Recombination

Electron recombination is also an important space-charge effect that needs to be taken into account in the simulation. For this effect, the electrons produced by ionizing particles in the gas volume may recombine with nearby ions due to electromagnetic interaction. For high-ionization densities, the recombination effect can induce significant losses in the collected charge. Two types of recombination processes are possible in the AT-TPC, columnar or volume recombination [37]. The columnar process is when an ion-electron pair produced in the same track recombines, while the volume process is a more general case where the ions are recombined with electrons from different tracks. Due to the relative strong fields and highly ionizing particles used in the AT-TPC, the columnar recombination is expected to be negligible in comparison with the volume recombination [36,37]. In the latter case, the recombination depends on the ionization rate $\dot{N}$, which can be approximated by Eq. (7). Thus, the recombination effect is beam-rate dependent. The time scale required for an ion-electron pair to recombine depends on the intrinsic properties of the gas expressed by the recombination coefficient α, which for a deuterium gas is $\alpha \sim 2.5\times10^{-6}$ cm^3/s [40].

The recombination loss in ionization chambers (parallel plate chambers) can be estimated as [41]

$$f = \frac{\alpha\dot{N}L^2}{6\mu^2E^2}, \tag{10}$$

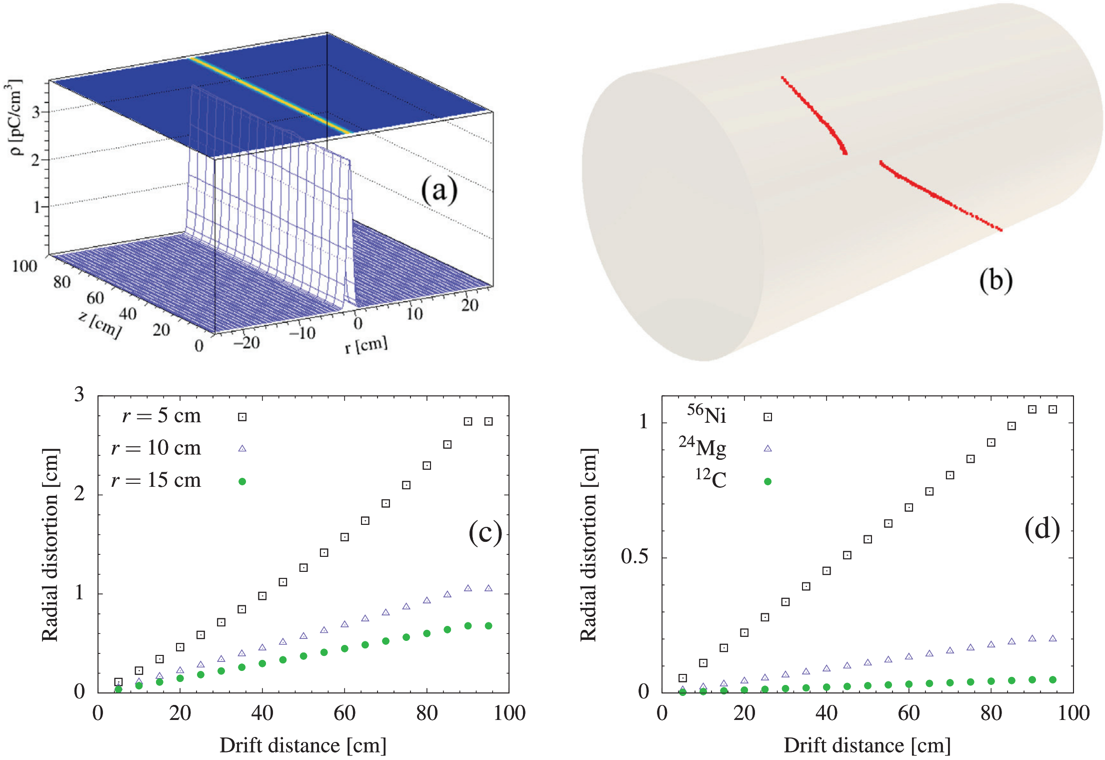

Fig. 8. (a) Charge distribution assumed in the model to describe the ion build-up. The distribution is a Gaussian profile extended along the active volume. (b) Simulated (d, ^{2}He) event including space-charge effects, in this case a 500 V/cm electric field was considered. An electric field component in the radial direction distorts the tracks close to the beam axis. For example, after a drift distance of 50 cm the radial distortion at the radii 5, 10 and 15 cm is 0.4, 0.2 and 0.1 cm. (c) Radial distortion as a function of the drift distance. The effects are stronger close to the beam axis. (d) Radial distortion as a function of the drift distance for three ion beams. The distortion effect increase with the ion-beam charge.

Table 1
Recombination loss and electron-ion production rate in a deuterium gas at 500 Torr and 500 V/cm. Three different beams were assumed at 100 MeV/u and 10^5 pps.

Ion beam	$\dot{N}$ [ions/(cm^3 s)]	f [%]
^{12}C	5.5×10^7	0.5
^{24}Mg	2.1×10^8	1.7
^{56}Ni	1.1×10^9	9.1

where μ is the ion mobility (≈13 cm^2/(V s) [37]), L is the AT-TPC length along the symmetry axis and E is the strength of the electric field. Eq. (10) provides an estimate value for the loss in charge collection assuming a constant beam rate impinging the gas target. As an example, Table 1 shows the recombination loss for three beams at 100 MeV/u and 10^5 pps interacting with a deuterium gas at 500 Torr and field strength of 500 V/cm.

As can be noticed, the recombination increases with the beam energy loss in the gas. As the recombination is expected to occur most likely near the beam region, the absolute effect may be a reduction in the space-charge build-up that distorts the electric field. For beam intensities above 10^6 pps, the recombination effect becomes significant and it is expected that part of the information of the tracks is lost [36].

4.3. *Correction*

The space-charge effects, mentioned in 4.1 and 4.2 can be corrected using a distortion map of the full active volume generated from simulations. As the beam impinges in central region of the active volume, space-charge effects can be assumed to be axially symmetric. This reduces the extraction of a distortion map to a two-dimensional problem. An electron transport routine including charge build-up and recombination effects was used to generate and transport electrons at different initial positions along the whole active volume. The relative distance of the electron cloud on the pad plane with respect to a given initial electron position defines the distortion. The distortion map was applied directly to the geometrical coordinates of each hit in order to restore the particle tracks. Fig. 9(a) shows a comparison of the reconstructed missing-mass energy for simulations with and without space-charge effects, and after the correction based on the distortion map. As can be seen, the energy resolution is strongly affected by the space charge mostly at high excitation energies. This effect can be related with a wrong determination of the reaction vertex and scattering angle of the protons. Similarly, the reconstruction efficiency of the ^{2}He particle is reduced by about 13% when the space-charge effects are included, i.e., 87% of the tracks can be restored with the present correction. This reduction in efficiency is because a few short tracks lose a fraction of their points in the central dead region (pad plane hole). However, with the correction, one is able to restore the energy resolution of the peaks. The minimum distance between the fitted proton tracks in the central region gives an estimate of how well the vertex can be reconstructed, see Fig. 9(b). The space-charge effects produce a wider distribution of the minimum distance between the two proton tracks that leads to a larger uncertainty in the determination of the vertex point. For this study, we chose the minimum distance between tracks to be less than 1 cm, which corresponds to about 2σ of the distorted track distribution. The correction improves the vertex reconstruction, which also impacts the missing-mass energy, as shown in Fig. 9(a). A similar procedure can be employed to correct experimental data. In this case, the distortion map might be extracted from simulations or from the same data by quantifying the distortion of the tracks in the full active volume.

5. Summary

A simulation and analysis code has been developed to study charge-exchange (d, ^{2}He) reactions in inverse kinematics using the AT-TPC.

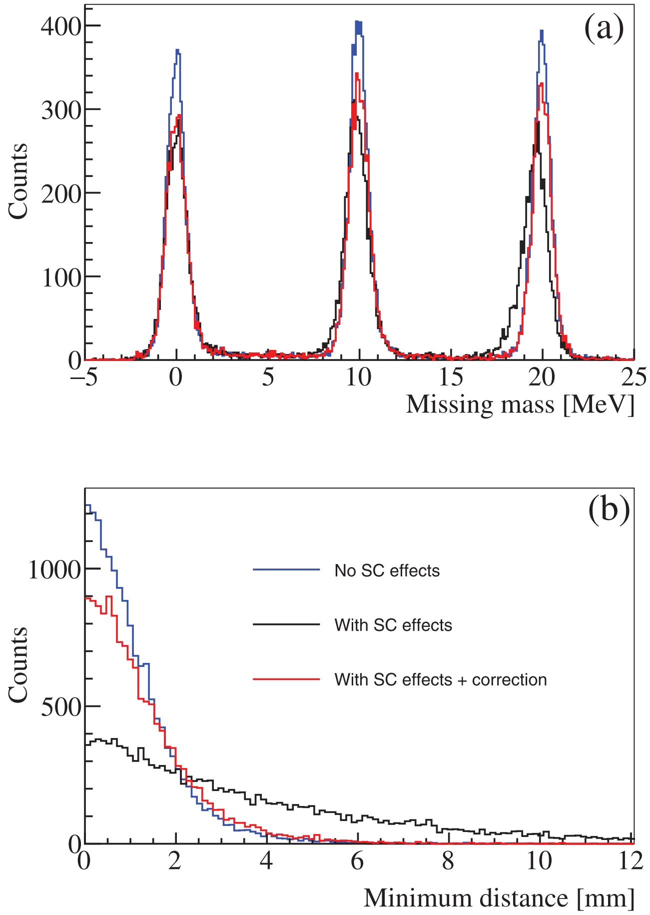

Fig. 9. Simulated ^{14}O(d,^{2}He) data with and without space-charge effects and the respective correction using a distortion map. (a) Reconstructed missing-mass energy. (b) Distribution of the minimum distance between the proton tracks. The meaning of the line color in both figures is the same.

The simulation package provides a realistic detector response that allows for processing the simulation output in the same manner as the experimental data. Dedicated subroutines for the event generator, digitization and reconstruction of nuclear reactions are used for simulating experiments with the AT-TPC. In particular, the event generator of $(d, {}^{2}\mathrm{He})$ reactions takes into account the production of two recoiling protons at low-momentum transfer with a relative energy, based on adiabatic coupled-channel calculations that are known to reproduce the dependence of the $(d, {}^{2}\mathrm{He})$ differential cross section on ε_{pp} and θ_{cm}. A point cloud of the reaction is obtained from the digitization of the proton tracks in the active gas volume. Pattern recognition and fitting algorithms are used for the analysis of the point clouds and for reconstructing the $(d, {}^{2}\mathrm{He})$ reactions. The missing-mass energy is very well reconstructed independently of the geometrical acceptance of the detector.

A few analysis tools were successfully tested with simulations. For instance, tracking algorithms with a better selection of proton tracks were employed to improve the detection efficiency of the ^{2}He particle decay. Detection of beam-like particles originating in $(d, {}^{2}\mathrm{He})$ reactions in inverse kinematics provides a better selectivity of the reaction channel and a strong background suppression. In this work, we investigated the use of a kinematic fitting procedure for improving the reconstruction of the reaction parameters. It was shown that the energy resolution of the excited states can be improved by about a factor 2 if beam tracking detectors are used. In the future, the kinematic fitting tool will provide a powerful method for data analysis in experiments with complete particle detection. Also, space-charge effects were investigated with a model that accounts for charge build-up and ion recombination. These effects are most relevant around the beam axis, and generate a distortion of the particle tracks in the central region. At relatively high beam intensities and large nuclear charge, the space-charge effects are expected to play a significant role in the deformation of the particle tracks. Therefore, the simulation model presented here was used to generate distortion maps that can be applied in the future to correct experimental data.

The analysis tools developed in this work are designed to process both simulated and experimental data. Future $(d, {}^{2}\mathrm{He})$ experiments in inverse kinematics using the AT-TPC will use the code. Many of the routines are also valid for the analysis of other type of reactions involving fast beams such as inelastic scattering and fission.

Declaration of competing interest

The authors declare that they have no known competing financial interests or personal relationships that could have appeared to influence the work reported in this paper.

Data availability

Data will be made available on request.

Acknowledgments

This work was supported by the US National Science Foundation under Grants PHY-2209429 (Windows on the Universe: Nuclear Astrophysics at FRIB), PHY-1430152 (JINA Center for the Evolution of the Elements). This material is based upon work supported by the U.S. Department of Energy, Office of Science, USA, Office of Nuclear Physics and used resources of the Facility for Rare Isotope Beams (FRIB), which is a DOE Office of Science User Facility, operated by Michigan State University, United States, under Award Number DE-SC0000661. This work has received financial support from Xunta de Galicia (Centro singular de investigación de Galicia accreditation 2019–2022), by European Union ERDF, and by the “María de Maeztu” Units of Excellence program MDM-2016-0692 and the Spanish Research State Agency. Y. A. acknowledges the support by the Spanish Ministerio de Economía y Competitividad through the Programmes “Ramón y Cajal” with the Grant No. RYC2019-028438-I.

References

[1] T. Kamae, et al., The TOPAZ time projection chamber, Nucl. Instrum. Methods Phys. Res. A 252 (2) (1986) 423–430, http://dx.doi.org/10.1016/0168-9002(86)91217-9.

[2] K. Ackermann, et al., The STAR time projection chamber, Nuclear Phys. A 661 (1) (1999) 681–685, http://dx.doi.org/10.1016/S0375-9474(99)85117-3.

[3] J. Alme, et al., The ALICE TPC, a large 3-dimensional tracking device with fast readout for ultra-high multiplicity events, Nucl. Instrum. Methods Phys. Res. A 622 (1) (2010) 316–367, http://dx.doi.org/10.1016/j.nima.2010.04.042.

[4] M. Heffner, et al., A time projection chamber for high accuracy and precision fission cross-section measurements, Nucl. Instrum. Methods Phys. Res. A 759 (2014) 50–64, http://dx.doi.org/10.1016/j.nima.2014.05.057.

[5] T. Furuno, et al., Performance test of the MAIKo active target, Nucl. Instrum. Methods Phys. Res. A 908 (2018) 215–224, http://dx.doi.org/10.1016/j.nima.2018.08.042.

[6] B. Mauss, et al., Commissioning of the ACtive TARget and time projection chamber (ACTAR TPC), Nucl. Instrum. Methods Phys. Res. A 940 (2019) 498–504, http://dx.doi.org/10.1016/j.nima.2019.06.067.

[7] R. Shane, et al., SπRIT: A time-projection chamber for symmetry-energy studies, Nucl. Instrum. Methods Phys. Res. A 784 (2015) 513–517, http://dx.doi.org/10.1016/j.nima.2015.01.026.

[8] J. Bradt, et al., Commissioning of the active-target time projection chamber, Nucl. Instrum. Methods Phys. Res. A 875 (2017) 65–79, http://dx.doi.org/10.1016/j.nima.2017.09.013.

[9] E. Koshchiy, et al., Texas Active Target (TexAT) detector for experiments with rare isotope beams, Nucl. Instrum. Methods Phys. Res. A 957 (2020) 163398, http://dx.doi.org/10.1016/j.nima.2020.163398.

[10] H. Ohnuma, et al., (d,^{2}He) reactions at E_d=260 MeV as a possible probe to nuclear spin-isospin excitation, Phys. Rev. C 47 (1993) 648–651, http://dx.doi.org/10.1103/PhysRevC.47.648.

[11] H. Okamura, et al., Tensor analyzing power of the (d,^{2}He) reaction at 270 MeV, Phys. Lett. B 345 (1) (1995) 1–5, http://dx.doi.org/10.1016/0370-2693(94)01607-E.

[12] H.M. Xu, et al., (d,^{2}He) reactions at E_d=125.2 MeV, Phys. Rev. C 52 (1995) R1161–R1165, http://dx.doi.org/10.1103/PhysRevC.52.R1161.

[13] S. Rakers, et al., Gamow-Teller matrix elements from the ^{12}C(d,^{2}He) and ^{24}Mg(d,^{2}He) reactions at 170 MeV, Phys. Rev. C 65 (2002) 044323, http://dx.doi.org/10.1103/PhysRevC.65.044323.

[14] D. Frekers, Facets of (d,^{2}He) charge-exchange reactions at intermediate energies, Nuclear Phys. A 731 (2004) 76–93, http://dx.doi.org/10.1016/j.nuclphysa.2003.11.020.

[15] S. Giraud, et al., β^+ Gamow-Teller strengths from unstable ^{14}O via the $(d,{}^2\mathrm{He})$ reaction in inverse kinematics, 2022, http://dx.doi.org/10.48550/ARXIV.2210.15866.

[16] Y. Ayyad, et al., Overview of the data analysis and new micro-pattern gas detector development for the Active Target Time Projection Chamber (AT-TPC) project, J. Phys. Conf. Ser. 876 (2017) 012003, http://dx.doi.org/10.1088/1742-6596/876/1/012003.

[17] Y. Ayyad, ATTPCROOT, 2022, https://github.com/ATTPC/ATTPCROOTv2.

[18] FairRoot Framework, https://github.com/FairRootGroup/FairRoot.

[19] I. Hřivnáĉová, The geant4 virtual monte carlo, J. Phys. Conf. Ser. 119 (3) (2008) 032025, http://dx.doi.org/10.1088/1742-6596/119/3/032025.

[20] S. Agostinelli, et al., Geant4—a simulation toolkit, Nucl. Instrum. Methods Phys. Res. A 506 (3) (2003) 250–303, http://dx.doi.org/10.1016/S0168-9002(03)01368-8.

[21] H. Okamura, Three-body treatment of the $(d,{}^2\mathrm{He})$ reaction on the basis of the adiabatic approximation, Phys. Rev. C 60 (1999) 064602, http://dx.doi.org/10.1103/PhysRevC.60.064602.

[22] D. Bazin, et al., The S800 spectrograph, Nucl. Instrum. Methods Phys. Res. B 204 (2003) 629–633, http://dx.doi.org/10.1016/S0168-583X(02)02142-0.

[23] C. Bäumer, et al., Determination of the Gamow-Teller strength distribution from the odd-odd nucleus ^{50}V measured through $^{50}\mathrm{V}(d,^2\mathrm{He})^{50}\mathrm{Ti}$ and astrophysical implications, Phys. Rev. C 71 (2005) 024603, http://dx.doi.org/10.1103/PhysRevC.71.024603.

[24] E.W. Grewe, et al., Gamow-Teller transitions to ^{32}P studied through the $^{32}\mathrm{S}(d,^2\mathrm{He})$ reaction at E_d = 170MeV, Phys. Rev. C 69 (2004) 064325, http://dx.doi.org/10.1103/PhysRevC.69.064325.

[25] S. Biagi, A multiterm Boltzmann analysis of drift velocity, diffusion, gain and magnetic-field effects in argon-methane-water-vapour mixtures, Nucl. Instrum. Methods Phys. Res. A 283 (3) (1989) 716–722, http://dx.doi.org/10.1016/0168-9002(89)91446-0.

[26] E. Pollacco, et al., GET: A generic electronics system for TPCs and nuclear physics instrumentation, Nucl. Instrum. Methods Phys. Res. A 887 (2018) 81–93, http://dx.doi.org/10.1016/j.nima.2018.01.020.

[27] Y. Ayyad, et al., Novel particle tracking algorithm based on the Random Sample Consensus Model for the Active Target Time Projection Chamber (AT-TPC), Nucl. Instrum. Methods Phys. Res. A 880 (2018) 166–173, http://dx.doi.org/10.1016/j.nima.2017.10.090.

[28] J. Zamora, G. Fortino, Tracking algorithms for TPCs using consensus-based robust estimators, Nucl. Instrum. Methods Phys. Res. A 988 (2021) 164899, http://dx.doi.org/10.1016/j.nima.2020.164899.

[29] J.F. Ziegler, et al., SRIM – The stopping and range of ions in matter (2010), Nucl. Instrum. Methods Phys. Res. B 268 (11) (2010) 1818–1823, http://dx.doi.org/10.1016/j.nimb.2010.02.091.

[30] S. Kox, et al., Cross section and deuteron analysing powers of the 1H(d, 2p)n reaction at 200 and 350 MeV, Nuclear Phys. A 556 (4) (1993) 621–640, http://dx.doi.org/10.1016/0375-9474(93)90473-B.

[31] S. Rakers, et al., Measuring the $(d,{}^2$He) reaction with the focal-plane detection system of the BBS magnetic spectrometer at AGOR, Nucl. Instrum. Methods Phys. Res. A 481 (1) (2002) 253–261, http://dx.doi.org/10.1016/S0168-9002(01)01365-1.

[32] P. Avery, Fitting Theory Writeups and References, http://www.phys.ufl.edu/~avery/fitting.html.

[33] A.G. Frodesen, O. Skjeggestad, H. Tofte, Probability and statistics in particle physics, Universitetsforlaget, Bergen, Norway, ISBN: 978-82-00-01906-0, 1979.

[34] R. Smith, J. Bishop, A fast universal kinematic fitting code for low-energy nuclear physics, Physics 1 (3) (2019) 375–391, http://dx.doi.org/10.3390/physics1030027.

[35] J. Park, FIT 70 - a Kinematic Fitting Routine, Stanford Linear Accelerator Center, Stanford University, 1972, http://dx.doi.org/10.2172/4599820.

[36] J. Randhawa, et al., Beam-induced space-charge effects in time projection chambers in low-energy nuclear physics experiments, Nucl. Instrum. Methods Phys. Res. A 948 (2019) 162830, http://dx.doi.org/10.1016/j.nima.2019.162830.

[37] M. Huyse, et al., Intensity limitations of a gas cell for stopping, storing and guiding of radioactive ions, Nucl. Instrum. Methods Phys. Res. B 187 (4) (2002) 535–547, http://dx.doi.org/10.1016/S0168-583X(01)01152-1.

[38] F. Böhmer, et al., Simulation of space-charge effects in an ungated GEM-based TPC, Nucl. Instrum. Methods Phys. Res. A 719 (2013) 101–108, http://dx.doi.org/10.1016/j.nima.2013.04.020.

[39] S. Rossegger, et al., Analytical solutions for space charge fields in TPC drift volumes, Nucl. Instrum. Methods Phys. Res. A 632 (1) (2011) 52–58, http://dx.doi.org/10.1016/j.nima.2010.12.213.

[40] M.A. Biondi, S.C. Brown, Measurement of electron-ion recombination, Phys. Rev. 76 (1949) 1697–1700, http://dx.doi.org/10.1103/PhysRev.76.1697.

[41] C.A. Colmenares, Bakeable ionization chamber for low-level tritium counting, Nucl. Instrum. Methods 114 (2) (1974) 269–275, http://dx.doi.org/10.1016/0029-554X(74)90544-8.